Carlo Giorgio Grlj, Nastia Degiuli, Ivana Martić, Tomislav Staroveški, Luka Berić, Ivan Heinrich*

Comparison of open water characteristics of scanned and generated propeller

University of Zagreb, Faculty of Mechanical Engineering and Naval Architecture, Ivana Lučića 5, Zagreb, 10000, Croatia
*Corresponding author: nastia.degiuli@fsb.unizg.hr

Original scientific paper
Received: January 15, 2026
Accepted: March 24, 2026
https://doi.org/10.65776/ep.20.4.2

Abstract

This study presents a numerical investigation of open water characteristics using propeller geometry obtained through different approaches: automated approach with an online generator and three-dimensional scanning. The main objective is to evaluate the influence of the chosen geometric modelling approach on the predicted propeller open water characteristics. The turbulent flow around the propeller is modelled using the steady incompressible Reynolds Averaged Navier-Stokes equations and Shear Stress Transport k-ω turbulence model in combination with the γ-$Re_{\theta t}$ transition model, enabling the simulation of both laminar and turbulent flow. Numerical simulations are performed using the commercial Computational Fluid Dynamics software STAR-CCM+ 2310. The methodology follows the recommendations of the International Towing Tank Conference, and verification of the numerical results is carried out through grid independence studies. Validation of the numerical results is performed by comparison with experimental open water data obtained at the Brodarski Institute in Zagreb. The open water characteristics predicted using the scanned and generated propeller are compared in terms of thrust, torque, and open water efficiency. The results provide insight into the sensitivity of propeller performance to geometric modelling approach and highlight the importance of accurate geometry representation in numerical analyses.

Keywords: *CFD, EFD, open water test, containership, Wageningen-B series*

1. Introduction

Computational Fluid Dynamics (CFD) is widely applied in marine engineering for the analysis of the hydrodynamic characteristics of marine propellers. This approach enables detailed investigation of the flow around a propeller without the need for costly and time-consuming towing tank tests. Recent studies have shown that CFD simulations can be used for accurate prediction of the Propeller Open Water (POW) characteristics.

In numerical simulations based on the Reynolds Averaged Navier-Stokes (RANS) equations, various approaches can be employed to simulate propeller operation, such as the overset mesh method [1, 2] or a steady-state approach based on a rotating coordinate system, commonly referred to as the Moving Reference Frame (MRF) method [3-6]. Numerical simulations allow researchers to study the hydrodynamic characteristics of propellers in open water conditions at different scales, thereby enabling investigation of scale effects on propeller performance. Chen et al. [1] investigated the scale effects on the highly skewed INSEAN E1619 propeller and observed a significant effect on the torque coefficient, as well as on pressure and velocity distributions, while the effect on the thrust coefficient was less pronounced. Specifically, at larger scales, higher non-dimensional pressure values were obtained on the suction side, whereas the opposite trend was observed on the pressure side. Dong et al. [4] studied the scale effects on the open water efficiency of the International Towing Tank Conference (ITTC) PPTC-II propeller. The authors observed influence of scale on the thrust coefficient and attributed it to the reduction of boundary-layer thickness on the propeller blades at full scale compared to model scale. Grlj et al. [6] investigated the scale effects on POW characteristics and demonstrated that they can be significantly reduced by applying a transition model. Emphasis was placed on the application of transition model at model scale, which enables improved prediction of laminar and turbulent flow near the propeller blades, thereby reducing discrepancies in the prediction of open water efficiency. The obtained results highlight the importance of careful selection of turbulence models to achieve high simulation accuracy. Studies addressing the application of transition models, particularly the $\gamma - \overline{Re}_{\theta t}$ transition model, indicate that this model improves the prediction of POW characteristics at model scale [7, 8]. By accounting for both laminar and turbulent flow, better agreement between the numerically obtained boundary-layer flow characteristics and experimental data has been achieved for both conventional and highly skewed propellers [9, 10]. Pawar and Brizzolara [11] showed that inclusion of a transition model at model scale improved agreement between numerical and experimental results for both conventional and ducted propellers. Lopes et al. [12] demonstrated that omission of additional terms describing crossflow leads to almost completely laminar flow around the propeller blades. When these terms are included, a significant portion of the flow becomes turbulent, resulting in reduced thrust and torque coefficients.

To obtain the 3D model of the propeller for use in the numerical simulations, different methods can be employed. It can be generated using automated tools such as the online generator for the Wageningen B-series propellers [13]. Another approach for obtaining the 3D model of a

propeller is reverse engineering if the physical propeller model is available. Guan and Gu [14] reconstructed the geometry of a propeller and a ship hull using point cloud data obtained from laser scanning of the surfaces. Njaastad et al. [15] automated the operation of an industrial robot to scan full-scale propeller blades using a high-precision camera and a laser sensor. The authors demonstrated that accurate propeller blade models can be obtained through automated scanning methods. In a more recent study, Njaastad et al. [16] presented a procedure for extracting various geometric parameters of propeller blades using point cloud data as input. The proposed method was validated by determining the propeller parameters for the KVLCC2 ship. Similarly, Zheng et al. [17] proposed a method for reconstructing propeller geometry from point cloud data.

In this study, CFD simulations are used to determine the hydrodynamic characteristics in open water of a Fixed Pitch Propeller (FPP). Numerical predictions of the POW characteristics obtained using a generated propeller geometry are compared with those obtained using a scanned propeller geometry. The remainder of the paper is organized as follows. Section 2 describes the case study, the experimental setup, the mathematical and numerical setup, and two approaches used to obtain the propeller geometry. Section 3 presents the numerical results, while Section 4 summarizes the main findings of the study.

2. Methods

2.1 Case study

The considered propeller is a FPP used for a post-Panamax 6750 TEU containership with the main parameters shown in Table 1.

Main Parameter	Value
Scale λ	35.18
Diameter, D	0.2075 m
Number of blades, Z	4
Expanded area ratio, A_E/A_0	0.75
Pitch ratio, P/D	0.8901
Hub ratio, d/D	0.1687
Rate of revolution, n	25.01 rps
Direction of rotation	Clockwise

Table 1. Propeller main parameters.

The 3D model of the propeller is obtained using two methods, which are explained in the subsection 2.5 in detail.

2.2 Experimental setup

The Open Water Tests (OWT) were conducted at the Brodarski Institute within the Croatian Science Foundation research project "Sustainable slow steaming for low-carbon shipping" [18]. The experimental results are taken from Degiuli et al. [19], where the authors provide a detailed description of the conducted OWT along with a comprehensive analysis of the associated experimental uncertainties. The OWT were conducted for advance coefficients J ranging from 0 to 1 by maintaining a constant rate of revolution and varying the advance speed v_A.

2.3 Mathematical formulation

The numerical simulations of the OWT are based on the RANS equations which read as follows:

$$\frac{\partial \overline{u}_i}{\partial x_i} = 0 \tag{1}$$

$$\rho \frac{\partial \overline{u}_i}{\partial t} + \rho \frac{\partial}{\partial x_j}(\overline{u}_i \overline{u}_j + \overline{u_i' u_j'}) = -\frac{\partial \overline{p}}{\partial x_i} + \frac{\overline{\tau}_{ij}}{\partial x_j} \tag{2}$$

where ρ is the fluid density, $\overline{u}_i$ is the averaged Cartesian component of the velocity vector, $\rho \overline{u_i' u_j'}$ is the Reynolds Stress Tensor (RST), $\overline{p}$ is the mean pressure, and $\overline{\tau}_{ij}$ is the mean viscous stress tensor.

The Shear Stress Transport k-ω (SSTKO) turbulence model is used for the closure of the governing equations. Two additional transport equations are solved: one for the turbulent kinetic energy k and one for the specific dissipation ω:

$$\frac{\partial}{\partial t}(\rho k) + \frac{\partial}{\partial x_i}(\rho k \overline{u}_i) = \frac{\partial^2 k}{\partial x_i^2}(\mu + \sigma_k \mu_t) + G_k + G_{nl} + \\ + G_b - \rho \beta^* f_{\beta^*}(\omega k - \omega_0 k_0) + S_k \tag{3}$$

$$\frac{\partial}{\partial t}(\rho \omega) + \frac{\partial}{\partial x_i}(\rho \omega \overline{u}_i) = \frac{\partial^2 \omega}{\partial x_i^2}(\mu + \sigma_\omega \mu_t) + G_\omega + D_\omega - \\ - \rho \beta f_\beta(\omega^2 - \omega_0^2) + S_\omega \tag{4}$$

where μ is the dynamic viscosity coefficient of the fluid, μ_t is the turbulent eddy viscosity, σ_k, σ_ω, β, and β^* are model coefficients, G_k, G_{nl}, G_b, and G_ω are the turbulent, non-linear, buoyancy, and specific dissipation production terms, respectively, f_{β^*} is the vortex-stretching modification factor, f_β is the free-shear modification factor, k_0 and ω_0 are the ambient values that counteract turbulence decay, and finally, S_k and S_ω are the user-specified source terms.

Since the numerical simulations are conducted at model scale, laminar flow is considered by implementing the $\gamma - \overline{Re}_{\theta t}$ transition model [6]. It consists of solving the transport equations for intermittency γ and transition momentum thickness Reynolds number $\overline{Re}_{\theta t}$, which read as follows:

$$\frac{\partial(\rho\gamma)}{\partial t}+\frac{\partial\left(\rho\overline{u}_j\gamma\right)}{\partial x_j}=P_\gamma-E_\gamma+\frac{\partial}{\partial x_j}\left[\left(\mu+\frac{\mu_t}{\sigma_f}\right)\frac{\partial\gamma}{\partial x_j}\right] \tag{5}$$

$$\frac{\partial\left(\rho\overline{Re}_{\theta t}\right)}{\partial t}+\frac{\partial\left(\rho\overline{u}_j\overline{Re}_{\theta t}\right)}{\partial x_j}=P_{\theta t}+ +\frac{\partial}{\partial x_j}\left[\sigma_{\theta t}\left(\mu+\mu_t\right)\frac{\partial\overline{Re}_{\theta t}}{\partial x_j}\right] \tag{6}$$

where P_γ and $P_{\theta t}$ are production terms, σ_f and $\sigma_{\theta t}$ are model coefficients, and E_γ is the destruction term.

The system of algebraic equations is obtained by discretizing the governing equations with the finite volume method. The rotation of the propeller is accounted for with the steady-state MRF method in which the region around the propeller is defined in a rotating coordinate system. The numerical simulations are performed until the thrust and torque converged for each *J*.

2.4 Numerical setup

The computational domain is cylinder shaped with the dimensions defined according to the ITTC recommendations [20]. The inlet boundary is positioned at 4*D* in front of the propeller and a uniform velocity inlet is defined as the boundary condition. The outlet boundary is set as pressure outlet, and it is positioned at 20*D* behind the propeller. The outer boundary is set at 4*D* from the propeller and symmetry boundary condition is used. The propeller surfaces are set as no-slip wall.

The computational domain is discretized using the hexahedral cells and the regions close to and behind the propeller are more refined. Prism layers are generated from the propeller surfaces to keep the non-dimensional wall distance y^+ below 1. This is because the boundary layer must be fully discretised for the transition model to activate. The computational domain and the generated mesh are shown in Figure 1.

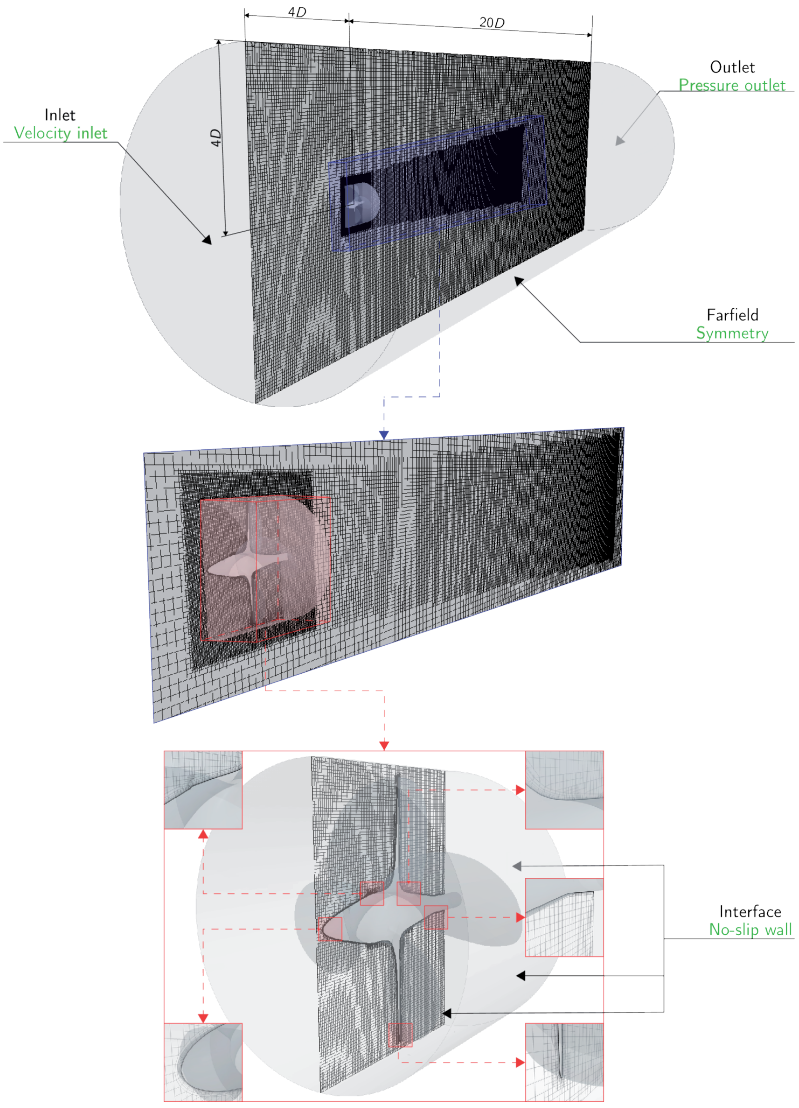

Fig. 1. The computational domain and the generated mesh.

The physical properties of water are set to freshwater conditions, consistent with the towing tank tests as: $\rho = 999.25\ \text{kg/m}^3$ and $\mu = 0.001191\ \text{Pa·s}$.

2.5 Geometry

The 3D model of the propeller was obtained using two methods: online generator and 3D scanning of the stock propeller. Since the analysed propeller is a Wageningen B-series propeller, the available online tool [13] was used for the generation of the 3D model of the propeller. To obtain the STL file of the 3D model, the only input required are the main parameters of the propeller. The graphical user interface is shown in Figure 2.

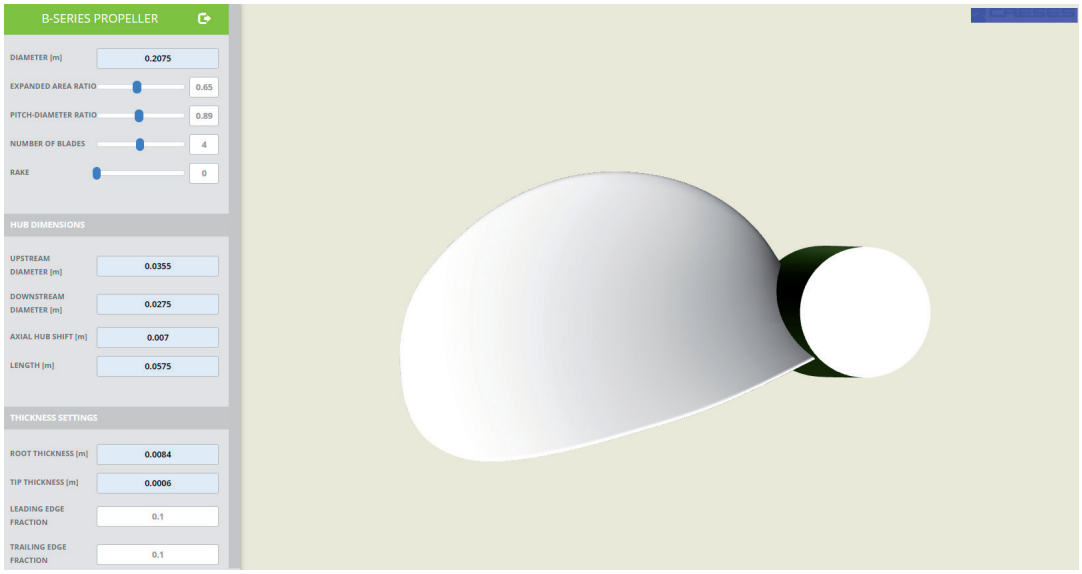

Fig. 2. Wageningen B-series online generator.

Since the stock propeller was available, the 3D scanning approach was employed using the ATOS 5x optical digitizer system [21]. The system comprises a scanning head equipped with a laser projector that generates a structured-light pattern. This pattern is projected onto the propeller surface and captured by high-resolution stereo cameras positioned at calibrated angles within the scanning head, as shown in Figure 3. To ensure measurement accuracy, the system incorporates real-time temperature compensation and adaptive exposure to account for environmental conditions and surface reflectivity variations. The resulting point cloud is generated through analysis and triangulation of the reflected light patterns using the Zeiss Inspect™ metrology software [22]. The propeller was coated with the surface treatment Reflecon Tarnish to obtain a uniform white surface, thereby improving the quality of the digitization process. The propeller was mounted on a rotating platform equipped with several uncoded circular markers with a diameter of 3 mm, as shown in Figure 4. Based on the acquired point cloud, a three-dimensional CAD model of the propeller was generated in STL format and subsequently smoothed for use in the numerical simulations.

Fig. 3. The 3D scanning process.

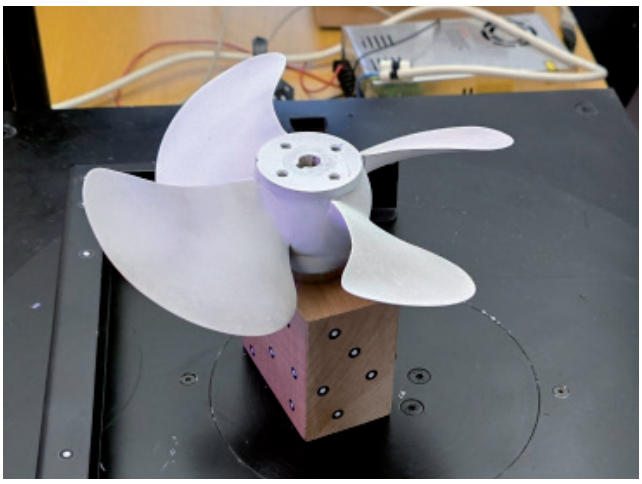

Fig. 4. The propeller situated on the rotating platform.

3. Results

3.1 Verification study

The verification study was performed to assess the numerical uncertainty due to mesh resolution using the Grid Convergence Index (GCI) method [23]. The calculation procedure for the *GCI* is provided by Grlj et al. [7]. It was necessary to calculate the grid spacing h to define the refinement ratio r between different mesh resolutions. Table 2 shows the obtained number of cells N and grid spacing h for each mesh size.

	Generated		Scanned	
	N	h, m	N	h, m
Coarse, 3	4.797M	9.00	1.734M	8.22
Medium, 2	6.088M	7.20	3.479M	5.81
Fine, 1	8.004M	5.83	8.001M	4.11

Table 2. Details of the meshes used in the verification study.

J	ε_{21}	ε_{32}	R	p	GCI_{fine}^{21}, %
0.08	0.0002	-0.0002	-1.36	0.877	0.83
0.16	0.0004	-0.0003	-1.17	0.448	1.52
0.24	0.0004	-0.0003	-1.39	0.956	0.43
0.32	0.0006	-0.0004	-1.45	1.062	0.46
0.40	0.0007	-0.0007	-1.04	0.125	4.40
0.48	0.0007	-0.0004	-1.85	1.775	0.18
0.56	-0.0004	-0.0005	0.70	1.038	0.18
0.64	-0.0004	-0.0005	0.73	0.908	0.19
0.72	-0.0006	-0.0009	0.71	0.997	0.27
0.80	-0.0019	-0.0026	0.73	0.908	0.89
0.88	-0.0053	-0.0056	0.95	0.145	23.89

Table 3. Results of the verification study for the generated propeller geometry.

The results of the verification study for the generated propeller geometry are shown in Table 3. The numerical uncertainty was calculated for the open water efficiency η_{O}. Monotonic convergence is achieved at $0.56 < J < 0.88$, while divergence is observed at lower J. The order of the method p is lower than 2, which suggests an overprediction of the *GCI*. Nevertheless, for most cases the calculated *GCI* is below 1 %, with only a few exceptions exhibiting higher values such as 1.51 % and 4.4 % at $J = 0.16$ and $J = 0.40$, respectively. The highest *GCI* is obtained at $J = 0.88$, however in this regime the η_{O} decreases rapidly. It should be noted that this operating region is not relevant to typical propeller performance, therefore, this point is considered an outlier and may be excluded from the verification study.

The results of the verification study for the scanned propeller geometry are shown in Table 4. Again, the numerical uncertainty was calculated for η_{O}. In this case, the obtained results are marginally better than those obtained for the generated propeller geometry. Monotonic convergence is obtained over almost the entire range of J. Slight oscillatory convergence is observed at $J = 0.08$, where p is well above 2, thus indicating an underprediction of the *GCI*. The obtained *GCI* is below 4 % for most cases, with the exception of the highest J, for which the *GCI* reaches 5.35 %. Excluding the lowest J, the minimum *GCI* value of 0.47 % is obtained at $J = 0.40$. Overall, both verification studies indicate that the fine mesh resolutions are adequate for the remaining numerical simulations.

J	ε_{21}	ε_{32}	R	p	GCI_{fine}^{21}, %
0.08	-0.00003	-0.0012	-0.03	10.569	0.001
0.16	-0.0010	-0.0018	0.55	1.711	0.82
0.24	-0.0018	-0.0023	0.79	0.696	2.96
0.32	-0.0018	-0.0031	0.57	1.603	0.79
0.40	-0.0018	-0.0038	0.49	2.090	0.47
0.48	-0.0027	-0.0043	0.63	1.324	1.07
0.56	-0.0036	-0.0050	0.73	0.927	1.94
0.64	-0.0042	-0.0059	0.72	0.944	2.04
0.72	-0.0048	-0.0067	0.71	0.982	2.07
0.80	-0.0070	-0.0097	0.72	0.942	3.10
0.88	-0.0098	-0.0132	0.74	0.864	5.35

Table 4. Results of the verification study for the scanned propeller geometry.

3.2 Validation study

In this subsection, the results of the validation study are presented. The relative deviations were calculated with the following equation:

$$RD = \frac{\phi_{\text{CFD}} - \phi_{\text{EFD}}}{\phi_{\text{EFD}}} \cdot 100\,\% \tag{7}$$

where ϕ is the considered physical quantity, and the subscripts CFD and EFD indicate that the results are obtained numerically and experimentally, respectively. First, the obtained results for both geometries and those obtained experimentally are compared in Figure 5. It is evident that the thrust coefficient K_T and torque coefficient K_Q obtained using the generated propeller geometry exhibit significant deviations from the experimental results. In contrast, numerical simulations performed with the scanned propeller geometry show improved agreement for both K_T and K_Q compared to those obtained with generated propeller geometry. However, the numerically predicted η_O differs significantly from the experimental values for both geometries, with the discrepancies increasing with J. The improved performance of the scanned geometry is attributed to the fact that, during the geometry generation process, certain input parameters had to be estimated due to the lack of precise measurements. Specifically, the authors did not have information on the rake angle, the leading and trailing edge fractions, or the size of the hub fillet. Moreover, the root and tip thicknesses were estimated based on the available drawings.

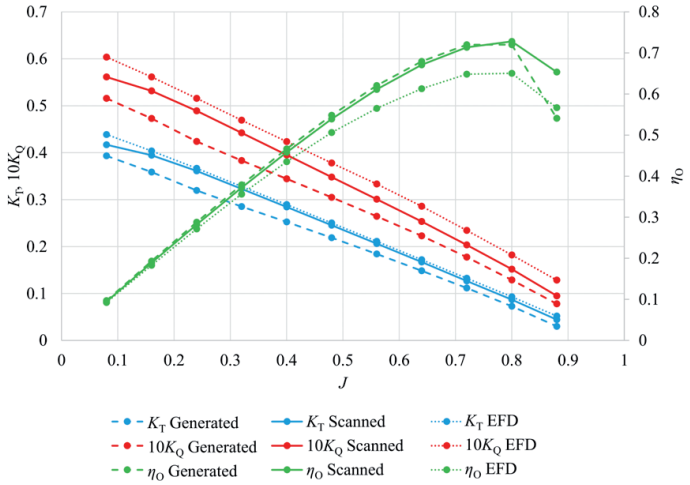

Fig. 5. Open water curves obtained numerically with generated and scanned propeller geometry, and experimentally.

The obtained relative deviations between the numerical and experimental results are given in Table 5. It can be seen that the relative deviations obtained between the numerical results with the generated propeller geometry and the experimental results are well above 10 % for both K_T and K_Q. The relative deviations for the scanned propeller are significantly lower than for the generated propeller. The relative deviations increase with J and the largest relative deviations are obtained for $J > 0.8$. However, this region is not relevant for typical propeller operating conditions.

	Generated			Scanned		
J	K_T, %	K_Q, %	η_O, %	K_T, %	K_Q, %	η_O, %
0.08	-10.38	-14.58	4.93	-4.99	-7.03	2.24
0.16	-11.13	-15.77	5.48	-2.24	-5.29	3.22
0.24	-12.83	-17.85	6.08	-1.49	-5.18	3.90
0.32	-13.07	-18.31	6.38	-1.64	-5.72	4.34
0.4	-12.84	-18.71	7.18	-1.82	-6.71	5.25
0.48	-12.67	-19.36	8.27	-2.00	-7.94	6.47
0.56	-12.8	-20.67	9.85	-2.29	-9.69	8.17
0.64	-13.62	-22.1	10.84	-2.89	-11.32	9.51
0.72	-15.85	-24.27	11.05	-4.39	-13.18	10.51
0.8	-21.56	-29.14	10.68	-6.65	-16.58	11.92
0.88	-42.03	-39.27	-4.61	-14.72	-26.03	15.27

Table 5. Relative deviations between the numerically and experimentally obtained results.

3.3 Flow visualization

In this subsection, more details of the obtained flow around the propeller at $J = 0.48$ are given. First, the obtained y^+ values on the propeller suction and pressure side are presented in Figure 6. For both geometries the y^+ values are below 1 across the entire propeller. In the case of the generated propeller geometry, y^+ values are marginally higher on the pressure side compared to those obtained for the scanned propeller geometry. This ensures that the boundary layer is fully resolved and that the transition model is active in the numerical simulations.

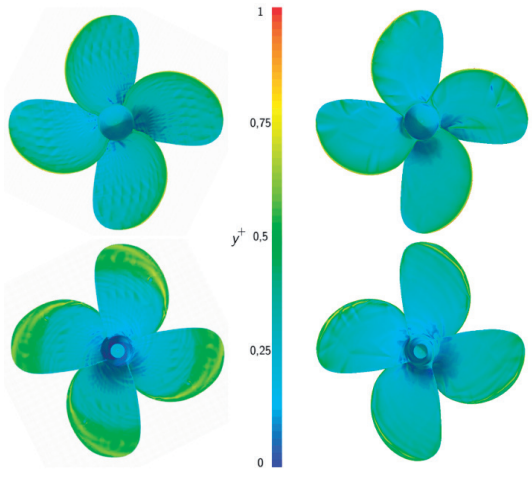

Fig. 6. The numerically obtained y^+ on the propeller suction (top) and pressure (bottom) side for generated (left) and scanned (right) propeller geometry.

Figure 7 presents the velocity magnitude distribution on the longitudinal cross section. It can be seen that the obtained velocity behind the propeller is higher in the case of the scanned propeller geometry compared to the generated propeller geometry. More details around the propeller are shown in Figure 8. The detailed view reveals that the transition between the blade and the hub is considerably smoother for the scanned propeller geometry than for the generated geometry. This is one of the factors contributing to the higher velocities observed downstream of the scanned propeller compared to those obtained with the generated propeller.

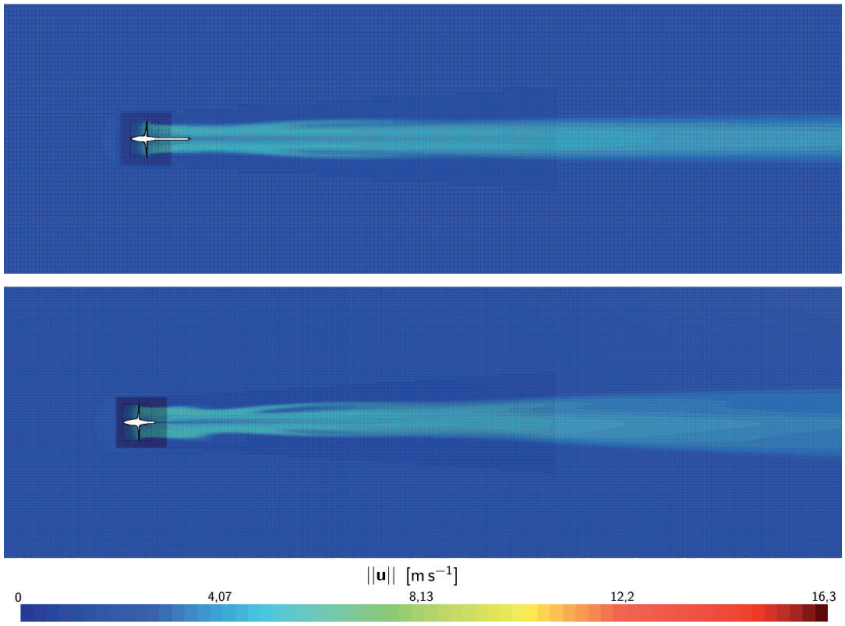

Fig. 7. The velocity magnitude on the longitudinal cross section obtained with the generated (top) and scanned (bottom) propeller geometry.

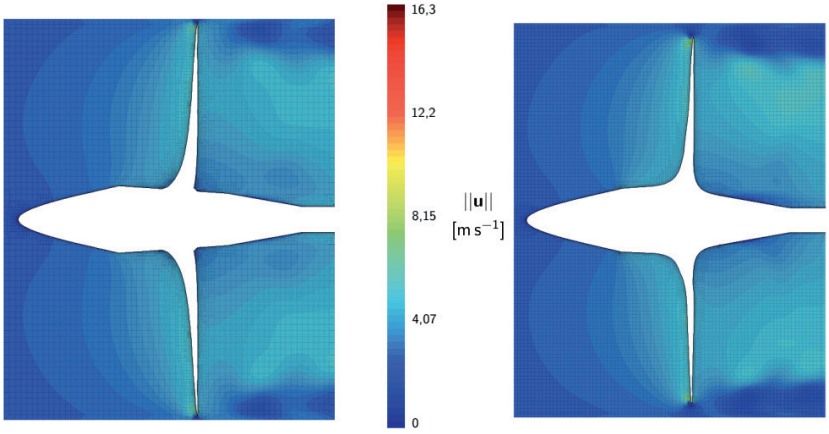

Fig. 8. Detailed view of the velocity magnitude around the generated (left) and scanned (right) propeller geometry.

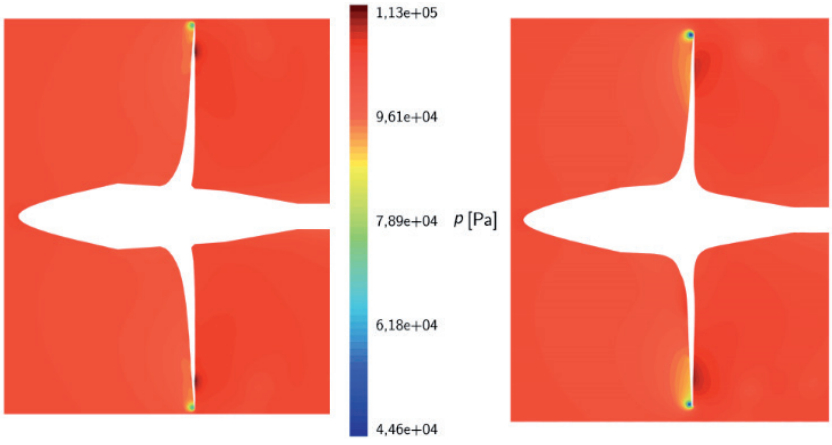

Fig. 9. Detailed view of the pressure around the generated (left) and scanned (right) propeller geometry.

Figure 9 shows the pressure fields around the propeller, with visible differences at the suction side on the propeller tips. Lower values are obtained for the scanned propeller compared to the generated propeller. Likewise, on the pressure side of the generated propeller the pressure is higher than for the case of the scanned propeller.

Lastly, the distribution of the skin friction coefficient C_f on the propeller surfaces are given in Figure 10. The differences between the results obtained with different propeller geometries are minimal. Slightly higher values of C_f are observed on the suction side of the scanned propeller compared to those of the generated propeller.

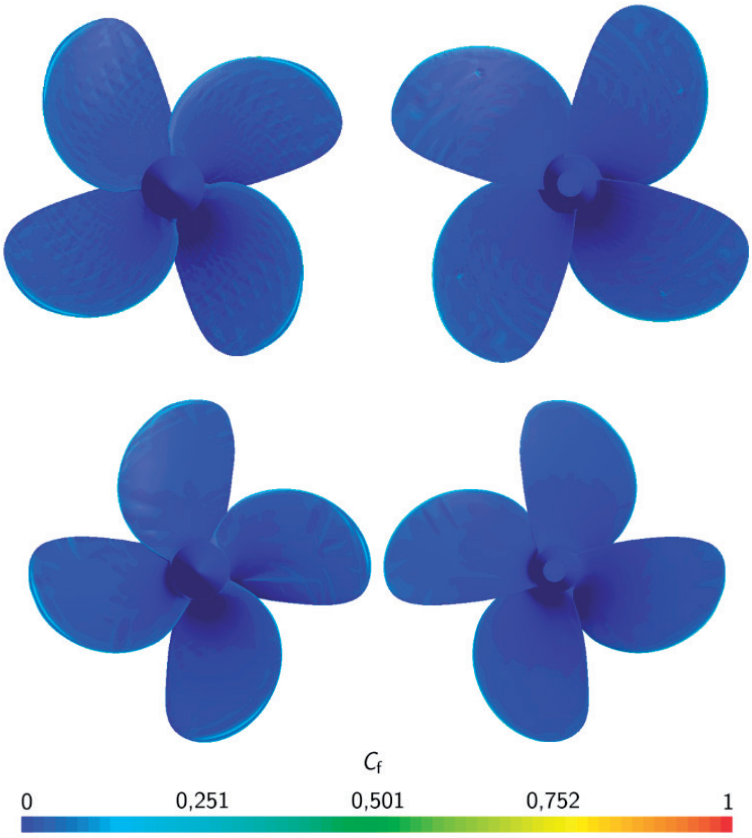

Fig. 10. Distributions of the skin friction coefficient on the suction (left) and pressure (right) side of the generated (top) and scanned (bottom) propeller geometry.

4. Conclusions

In this study, numerical simulations were performed to determine the open water characteristics for generated and scanned propeller. The mathematical model is based on the Reynolds Averaged Navier-Stokes equations and employs the Shear Stress Transport k-ω turbulence model in combination with the γ-$Re_{\theta t}$ transition model. The computational domain is discretized using the finite volume method within the commercial CFD software STAR-CCM+ 2310.

Two approaches to propeller geometry generation are considered: an automated approach with an online generator and 3D scanning of a stock propeller model. Verification of the numerical simulations is carried out using the Grid Convergence Index method. The verification procedure is applied for the open water efficiency of both propellers for the range of advance coefficient from 0.08 to 0.88. For the generated propeller, most *GCI* values are below 1 %, whereas slightly higher *GCI* values are observed for the scanned propeller. This confirms that the fine meshes are adequate for the rest of the numerical simulations.

Validation of the numerical results is performed through comparison with experimental data obtained at the Brodarski Institute in Zagreb. The results show that numerical simulations with the scanned propeller exhibit better agreement with the experimental data than those based on the generated propeller with respect to the thrust and torque coefficients. A direct comparison between the generated and scanned propeller reveals significant discrepancies in the thrust and torque coefficients, while the differences in open water efficiency are relatively small. These findings clearly indicate that the details of the actual propeller geometry have a substantial impact on the accuracy of numerical predictions.

Overall, this analysis confirms that computational fluid dynamics can be used to efficiently and reliably predict the propeller open water characteristics, provided that the propeller geometry is defined with sufficient accuracy.

5. Acknowledgement

This work was supported by the Croatian Science Foundation under the project number IP-2025-02-4779.

6. References

[1] Chen, X., Huang, Y., Wei, P., Zhang, Z., Jin, F. Numerical analysis of scale effect on propeller E1619. Proc. Int. Conf. Offshore Mech. Arct. Eng. - OMAE, 7B (2018)

[2] Shen, Z., Wan, D., Carrica, P. M. Dynamic overset grids in OpenFOAM with application to KCS self-propulsion and maneuvering. Ocean Eng. 108 (2015) 287-306

[3] Dogrul, A. Numerical prediction of scale effects on the propulsion performance of Joubert BB2 submarine. Brodogradnja 73(2) (2022) 17-42

[4] Dong, X. Q., Li, W., Yang C. J., Noblesse, F. RANSE-based simulation and analysis of scale effects on open-water performance of the PPTC-II benchmark propeller. J. Ocean Eng. Sci. 3(3) (2018) 186-204

[5] Farkas, A., Degiuli, N., Martić, I. The impact of biofouling on the propeller performance. Ocean Eng. 219 (2021) 108376

[6] Grlj, C. G., Degiuli, N., Farkas, A., Martić, I. Numerical Study of Scale Effects on Open Water Propeller Performance. J. Mar. Sci. Eng. 10(8) (2022) 1132

[7] Grlj, C. G., Degiuli, N., Martić, I. The Impact of Numerical Parameters on the Resistance Characteristics of a Container Ship at the Model and Full Scale. J. Mar. Sci. Eng. 11(9) (2023) 1672

[8] Grlj, C. G., Degiuli, N., Martić, I. Scale effects on the resistance and propulsion characteristics of the Japan Bulk Carrier. Ocean Eng. 339 (2025), 122059

[9] Liu, B., Vanierschot, M., Buysschaert, F. Comparison Study of the k − kL − ω and γ − Reθ Transition Model in the Open-Water Performance Prediction of a Rim-Driven Thruster. Int. J. Turbomach. Propuls. Power 9(1) (2024) 2

[10] Baltazar, J., Rijpkema, D., Falcão de Campos, J. On the use of the γ-Reθt transition model for the prediction of the propeller performance at model-scale. Ocean Eng. 170 (2018) 6-19

[11] Pawar, S., Brizzolara, S. Relevance of transition turbulent model for hydrodynamic characteristics of low Reynolds number propeller. Appl. Ocean Res. 87 (2019) 165-178

[12] Lopes, R., Eslamdoost, A., Johansson, R., RoyChoudhury, S., Bensow, R. E. A numerical study on the influence of crossflow transition on a marine propeller in open water. Ocean Eng. 310 (2024) 118573

[13] A. Friendship Systems. B-Series Propeller Generator.

URL:https://www.wageningen-b-series-propeller.com (23.1.2025.)

[14] Guan, G., Gu, W. Reconstruction of propeller and complex ship hull surface based on reverse engineering. J. Mar. Sci. Technol. 27(6) (2019) 0002

[15] Njaastad, E. B., Munthe-Kaas, N. H. Egeland, O. Robotic Autoscanning of Highly Skewed Ship Propeller Blades. IFAC-PapersOnLine 51(22) (2018) 435-440

[16] Njaastad, E. B., Steen, S., Egeland, O. Identification of the geometric design parameters of propeller blades from 3D scanning. J. Mar. Sci. Technol. 27(2) (2022) 887-906

[17] Zheng, L., Chen, S., Chen, X., Ji, S. Reverse Engineering-Inspired Parametric 3D Geometry Model of Marine Propeller. Pol. Marit. Res. 30(3) (2023) 35-47

[18] Brodarski Institute, "Report 6655-M. Resistance, self-propulsion and 3D wake measurement test results," Zagreb, 2022

[19] Degiuli, N., Martić, I., Pedišić-Buča, M., Grlj, C. G. Benchmark study on resistance and propulsion characteristics of a 6750-TEU container ship. Ocean Eng. 319 (2025) 120300

[20] ITTC, "Practical Guidelines for Ship Self-Propulsion CFD, ITTC 7.5-03-03-01.," ITTC-Recommended Procedures and Guidelines (2014)

[21] Zeiss. ATOS 5X.
URL: https://www.zeiss.com/metrology/en/systems/optical-3d/3d-scanning/atos/atos-5x.html (29.1.2025.)

[22] Zeiss. ZEISS Inspect.
URL: https://www.zeiss.com/metrology/en/software/zeiss-inspect.html (29.1.2025.)

[23] Eça, L., Hoekstra, M. A procedure for the estimation of the numerical uncertainty of CFD calculations based on grid refinement studies. Journal of Computational Physics. 262 (2014) 104-13